

Variation between Antiferromagnetism and Ferrimagnetism in NiPS₃ by Electron Doping

Mengjuan Mi^{1#}, Xingwen Zheng^{2#}, Shilei Wang^{3#}, Yang Zhou², Lixuan Yu¹, Han Xiao¹, Houning Song², Bing Shen⁴, Fangsen Li⁵, Lihui Bai², Yanxue Chen^{2*}, Shanpeng Wang^{3*}, Xiaohui Liu^{2*}, Yilin Wang^{1*}

¹School of Microelectronics, Shandong Technology Center of Nanodevices and Integration, State Key Laboratory of Crystal Materials, Shandong University, Jinan 250100, China.

²School of Physics, Shandong University, Jinan 250100, China.

³State Key Laboratory of Crystal Materials, Institute of Crystal Materials, Shandong University, Jinan, 250100, China.

⁴School of Physics, Sun Yat-Sen University, Guangzhou 510275, China.

⁵Vacuum Interconnected Nanotech Workstation, Suzhou Institute of Nano-Tech and Nano-Bionics, Chinese Academy of Sciences, Suzhou 215123, China.

[#]These authors contributed equally.

*Correspondence and requests for materials should be addressed to: Y.W. (email: yilinwang@email.sdu.edu.cn); X.L. (liuxiaohui@sdu.edu.cn); S.W. (wshp@sdu.edu.cn); Y.C. (cyx@sdu.edu.cn)

Abstract:

How to electrically control magnetic properties of a magnetic material is promising towards spintronic applications, where the investigation of carrier doping effects on antiferromagnetic (AFM) materials remains challenging due to their zero net magnetization. In this work, we found electron doping dependent variation of magnetic orders of a two-dimensional (2D) AFM insulator NiPS₃, where doping concentration is tuned by intercalating various organic cations into the van der Waals gaps of NiPS₃ without introduction of defects and impurity phases. The doped NiPS₃ shows an AFM-ferrimagnetic (FIM) transition at doping level of 0.2-0.5 electrons/cell and a FIM-AFM transition at doping level of ≥ 0.6 electrons/cell. We propose that the found phenomenon is due to competition between Stoner exchange dominated inter-chain ferromagnetic order and super-exchange dominated inter-chain AFM order at different doping level. Our studies provide a viable way to exploit correlation between electronic structures and magnetic properties of 2D magnetic materials for realization of magnetoelectric effect.

1. Introduction

Since the first experimental observation of intrinsic ferromagnetism in monolayer CrI_3 ¹ and bilayer $\text{Cr}_2\text{Ge}_2\text{Te}_6$ ², van der Waals (vdW) magnetic materials have attracted extensive attention in both fundamental research and practical applications³⁻⁹. The field of two-dimensional (2D) magnetic materials grows rapidly and various types of 2D magnetic materials have been discovered and synthesized, such as ferromagnetic (FM) magnets including $\text{Cr}_2\text{Ge}_2\text{Te}_6$ ², CrBr_3 ¹⁰, Fe_3GeTe_2 ^{11,12}, Fe_5GeTe_2 ¹³, monolayer VSe_2 ¹⁴, etc., and antiferromagnetic (AFM) magnets including CrCl_3 ¹⁵, transition metal phosphorous trichalcogenides MPX_3 ($\text{M} = \text{Mn}, \text{Fe}, \text{Ni}; \text{X} = \text{S}, \text{Se}$)¹⁶⁻¹⁹, CrPS_4 ²⁰, MnBi_2Te_4 ²¹, etc. The distinct spin-dependent properties of these materials provide a promising platform for the discovery and study of new quantum phenomena and design of novel spintronic devices.

Due to the ultrathin thickness and weak interlayer vdW interaction of 2D magnetic materials, their magnetic properties, such as Curie temperature, magnetic anisotropy, saturation magnetization, and coercive force can be effectively modulated by magnetic field¹, electric field²², strain²³, electrostatic doping^{11,24-27}, and ion intercalation²⁸, etc. Several studies have demonstrated the carrier doping dependent changes in magnetic properties of CrI_3 ²⁴, $\text{Cr}_2\text{Ge}_2\text{Te}_6$ ^{26,28}, and Fe_3GeTe_2 ¹¹, which are attributed to carrier doping induced change on exchange interaction due to orbital occupation of transition metal atoms in these materials. The modulation of magnetic properties by carrier doping serves as a viable tool for realizing effective magnetoelectric coupling and is promising for designing electric-field controlled spintronic devices. However, among these impressive studies, experimental realization of carrier doping induced AFM-FM transition in 2D magnetic materials has rarely been reported²⁴ and the mechanism responsible for the magnetic transition is not clear and needs to be further explored.

Among various magnetic materials, MPX_3 compounds are of great interest for their rich variety of electronic and magnetic properties depending on the role of the transition metal elements^{16-19,29,30}: Heisenberg-type MnPS_3 , Ising-type FePS_3 , and XY or XXZ-type NiPS_3 . MPX_3 compounds have been theoretically predicted to exhibit

strong charge-spin coupling^{31,32} and carrier doping dependent AFM-FM transition^{33,34}, while experimental studies are lack.

In this work, we report on the electron doping dependent AFM-FIM transition in a self-doped AFM insulator NiPS₃, where the electron doping is realized by intercalating organic cations into the van der Waals gaps³⁵. Intercalation has been demonstrated to be an effective method to dope electrons into 2D materials and modulate their electronic, optical, magnetic, and superconducting properties^{28,36-40}. We found variation of magnetic order from AFM to FIM and then AFM with the increasing of electron concentration. Our experimental results are consistent with theoretical analysis based on the first-principles calculations. We propose that such AFM-FIM transition at low electron doping level originates from the Stoner exchange due to the self-doped feature of NiPS₃ which provides effective inter-chain itinerant channel. The FIM-AFM transition at high electron doping level is due to the rise of inter-chain superexchange. Our studies provide a new insight into the carrier doping tuned magnetic transition in 2D magnetic materials.

2. Results and Discussion

Figure 1(a) shows the crystal and magnetic structures of NiPS₃^{29,30,41,42}. Bulk NiPS₃ has a monoclinic structure (*C2/m*), where two P atoms (P-P pair) are covalently bonded to six S atoms to form a (P₂S₆)⁴⁻ anion complex, and each Ni atom carries a +2 electronic ionization state and lies on a honeycomb lattice in the *ab* plane. The layers in the *ab* plane are coupled by weak vdW interactions along the *c*-axis, and the interlayer distance is 6.34 Å. Below Néel temperature ($T_N \sim 150$ K), magnetic moments are aligned mostly in the *ab* plane (along the *a*-axis direction) with a small out-of-plane component, and each Ni²⁺ ion is coupled ferromagnetically to two of the nearest neighbors and antiferromagnetically to the third one, forming zigzag ferromagnetic chains (parallel to the *a*-axis) coupled antiferromagnetically to each other along the *b*-axis direction (zigzag AFM order, upper panel in Figure 1(a)). The non-equivalent Ni²⁺ ions in two adjacent ferromagnetic zigzag chains are marked as Ni(1) and Ni(2), respectively.

Intercalation offers a versatile approach for tuning charge carriers in 2D materials due to the charge transfer between guest intercalants and host 2D materials³⁵. Because of the remarkable wide vdW gap in MPX₃, guest intercalants can be easily intercalated into the vdW gaps, and these compounds have been extensively studied as cathodic materials in lithium batteries⁴³. High-quality NiPS₃ bulk crystals were used as the host materials, and electrochemical intercalation method was adopted to insert organic cations, such as THA⁺, into the vdW gaps of NiPS₃, as shown in Figure 1(a). The successful intercalation is confirmed by X-ray diffraction (XRD) measurement as shown in Figure 1(b), where the obvious shift of diffraction peaks to smaller angles indicates that the interlayer distance is expanded to 14.69 Å.

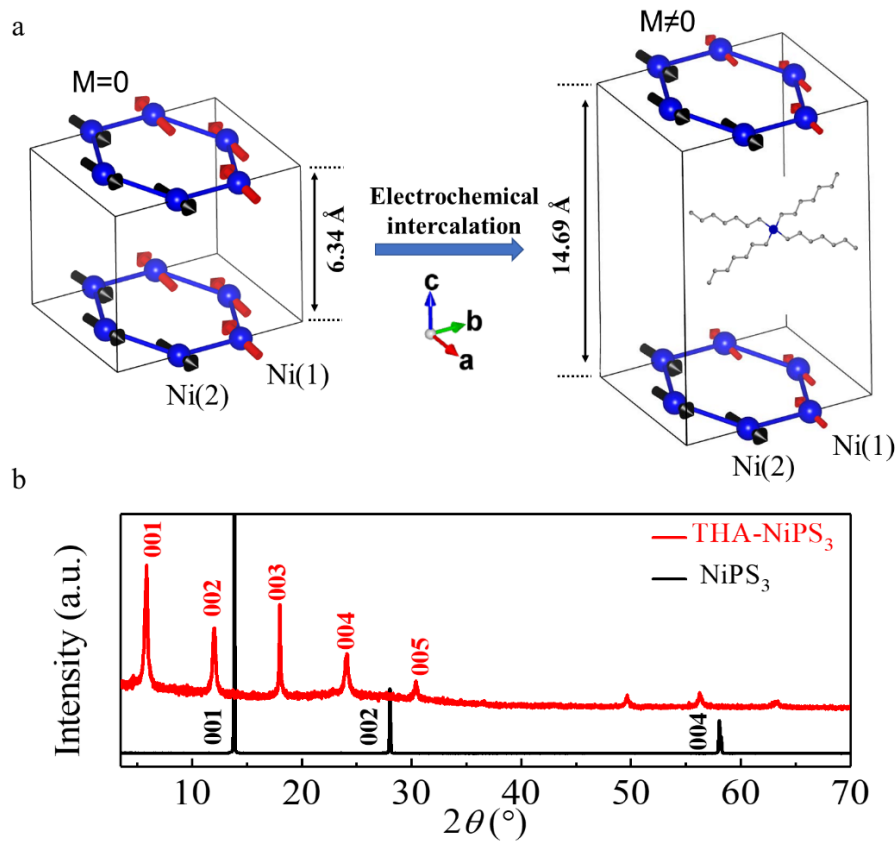


Fig. 1 Structures of pristine NiPS₃ and intercalated THA-NiPS₃. **a** Structures of NiPS₃ (left) and THA⁺ cations intercalated NiPS₃ (THA-NiPS₃, right). Arrows indicate the orientation and size of magnetic moments of Ni atoms, and the Ni atoms in two adjacent zigzag ferromagnetic chains are marked as Ni(1) and Ni(2), respectively. **b** XRD patterns of pristine NiPS₃ and intercalated THA-NiPS₃.

Figure 2 shows the temperature-dependent magnetization (M - T) and field-dependent magnetization (M - H) for pristine NiPS₃ and intercalated THA-NiPS₃ with a magnetic field applied along directions parallel to the ab plane and perpendicular to the ab plane (c^*). The overall behavior of pristine NiPS₃ is consistent with previous results, and a typical AFM characteristic is observed^{29,30}. No substantial difference is observed between the field-cooled (FC) and zero-field cooled (ZFC) measurements. The broad maximum at elevated temperatures is related to the short-range spin correlations. The Néel temperature, T_N , defined from the sharp peak in the derivative dM/dT for $H // ab$ is ~ 150 K (inset of Figure 2(a)). Below T_N , with respect to the magnetization for $H // c^*$, the magnetization for $H // ab$ decreases rapidly and reaches a smaller value at low temperature (Figure 2(a)), indicating that the magnetic moments lie mostly in the ab plane. A linear dependence of M vs H for $H // c^*$ is observed, while a clear upturn in M vs H for $H // ab$ above a critical field $\mu_0 H \sim 5$ T is observed (Figure 2(b)). The upturn in the magnetization at high field may be attributed to the spin-flop transition in pristine NiPS₃⁴⁴.

After intercalation, an obvious FIM characteristic (discuss in detail later) with a Curie temperature $T_c \sim 100$ K is observed in THA-NiPS₃. As shown in Figures 2(c)-2(d), for $H // ab$, the magnetization increases rapidly below 100 K, and an obvious magnetic hysteresis loop is observed at a low temperature, which provides an unambiguous identification of FIM order. For $H // c^*$, the magnetization is significantly smaller, and a linear dependence of M vs H is observed, which suggests that the large magnetic anisotropy still remains in intercalated THA-NiPS₃, and the FIM easy axis still lies in the ab plane. With increasing temperature (Figures 2(e)-2(f)), the magnetic hysteresis loop becomes less obvious, and both remnant magnetization and coercive field become smaller monotonically. The M - H curve shows a linear dependence at $T = 100$ K (inset in Figure 2(e)), indicating a FIM-paramagnetic transition, which is consistent with the M - T curves in Figure 2(c).

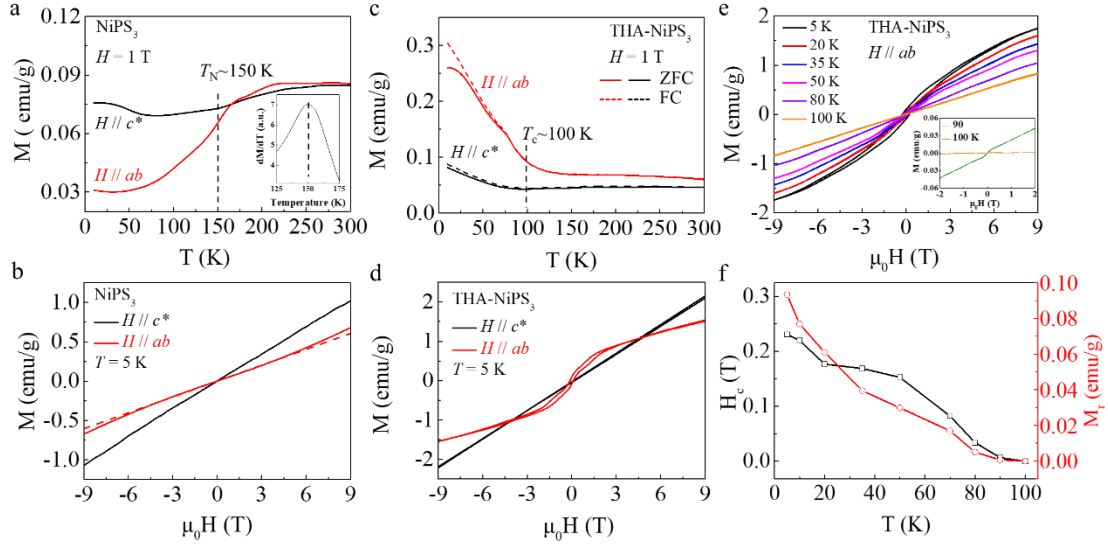


Fig. 2 Magnetic properties of pristine NiPS₃ and intercalated THA-NiPS₃. **a, b** Temperature dependence of magnetization (M - T , **a**) in zero-field cooled (ZFC) mode and field dependence of magnetization (M - H , **b**) of pristine NiPS₃ under magnetic fields $H // ab$ (red) and $H // c^*$ (black). **c, d** Temperature dependence of magnetization (M - T , **c**) and field dependence of magnetization (M - H , **d**) of intercalated THA-NiPS₃ under magnetic fields $H // ab$ (red) and $H // c^*$ (black). The solid and dashed lines in **c** represent zero-field cooled (ZFC) and field cooled (FC) data, respectively. **e** Isothermal magnetization of intercalated THA-NiPS₃ under a magnetic field $H // ab$ at different temperatures. Inset shows enlarged M - H data at 90 K and 100 K after subtracting a linear fitting. **f** Extracted remnant magnetization M_r (red) and coercive field H_c (black) of intercalated THA-NiPS₃ as a function of temperature.

What causes the magnetic transition from AFM in pristine NiPS₃ to FIM in intercalated THA-NiPS₃? Whether such AFM-FIM transition originates from defects or impurity phases? To solve these puzzles, detailed structural and chemical characterizations were carried out. Figure 3 shows typical morphologies of exfoliated pristine NiPS₃ and intercalated THA-NiPS₃ thin flakes. The intercalated THA-NiPS₃ has a flat and smooth surface, and no obvious defects are observed. After intercalation, the root-mean-square (RMS) roughness slightly increases from 0.2 nm (pristine NiPS₃) to 0.35 nm (THA-NiPS₃). A step height of ~ 1.6 nm is observed for THA-NiPS₃ (see supplementary Fig. S1), which is consistent with the XRD results. We provided the first experimental evidence showing that the organic cations intercalated 2D materials host a platform for the atomic-scale investigation by scanning probe techniques.

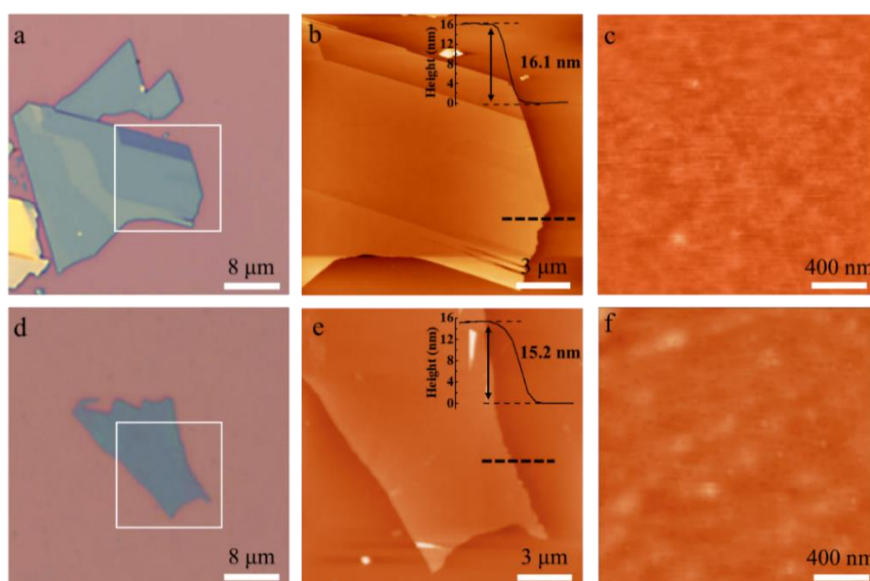


Fig. 3 Surface morphologies of pristine NiPS₃ and intercalated THA-NiPS₃. **a-c** Optical image (a), AFM image (b) and zoomed-in AFM image (c) of exfoliated pristine NiPS₃. **d-f** Optical image (d), AFM image (e) and zoomed-in AFM image (f) of exfoliated intercalated THA-NiPS₃. Insets in **b** and **e** indicate the thickness line profiles of pristine NiPS₃ and intercalated THA-NiPS₃, respectively.

We investigate whether defects are formed in intercalated THA-NiPS₃ by Raman spectroscopy, which is an eminent technique for the characterization of many properties, such as the number of layers, strain, disorder, and defect density, etc., of 2D materials⁴⁵. Figure 4(a) compares the Raman spectra of bulk pristine NiPS₃ and bulk intercalated THA-NiPS₃. Eight Raman-active phonon modes (three out-of-plane A_{1g} modes and five in-plane E_g modes) are observed in pristine NiPS₃, which is consistent with previous results¹⁶. For intercalated THA-NiPS₃, most peaks of pristine NiPS₃ are still observed, and a new peak near 206 cm⁻¹ that is absent in bulk pristine NiPS₃ appears. This peak is ascribed to the resonance-enhanced multi-phonon scattering, and is only observed in ultrathin NiPS₃ flakes^{16,42}. The evolution of three out-of-plane modes (A_{1g}¹, A_{1g}², and A_{1g}³, which are sensitive to interlayer coupling) of NiPS₃ after intercalation is consistent with the results of pristine NiPS₃ as thickness decreases (see supplementary Fig. S2)⁴². The Raman spectroscopy of intercalated THA-NiPS₃ is very similar to that of exfoliated monolayer NiPS₃¹⁶, and no signature related to defects and strain was observed, indicating that the intercalated organic cations effectively reduce interactions between adjacent layers without breaking the in-plane covalent bonds.

We further investigate whether impurity phases are formed in intercalated THA-NiPS₃ by X-ray photoelectron spectroscopy (XPS), which identifies the chemical shift caused by electron state surrounding the atoms of NiPS₃ after intercalation, and the results are shown in Figure 4(b). For pristine NiPS₃, the Ni 2p spectrum consists of two main peaks located at binding energies of 854.5 eV and 871.8 eV accompanied with satellite peaks, which correspond to 2p_{3/2} and 2p_{1/2} levels, respectively. After intercalation, both Ni 2p_{3/2} and Ni 2p_{1/2} peaks obviously shift towards lower binding energies and the intensities of the satellite peaks are weakened, which is consistent with the results in lithium intercalated NiPS₃ (Li_xNiPS₃)⁴⁶. Similarly, both P 2p spectrum (2p_{3/2} and 2p_{1/2}) and S 2p spectrum (2p_{3/2} and 2p_{1/2}) shift towards lower binding energies after intercalation (see supplementary Table 1). No signature indicative of impurity phases was observed, and the shift of XPS peaks towards lower binding energies clearly indicates that the intercalation of THA⁺ cations leads to electron doping³⁵.

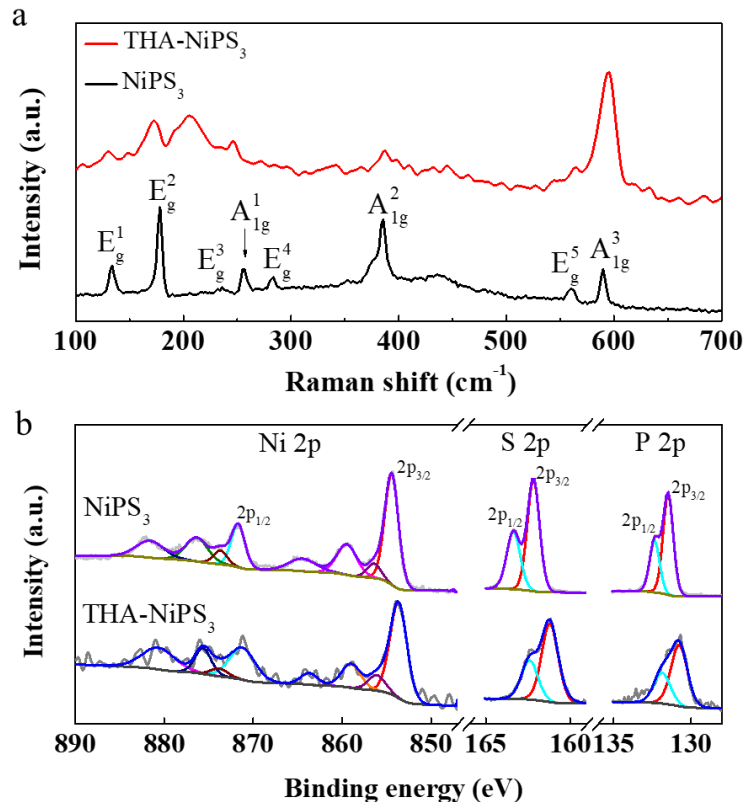


Fig. 4 Raman (a) and XPS (b) spectra of pristine NiPS₃ and intercalated THA-NiPS₃.

The intercalated THA^+ cations decouple the interactions between adjacent NiPS_3 layers and lead to electron doping of NiPS_3 without introducing obvious strain, defects, and impurities phases. To understand the effects of electron doping on the electronic and magnetic properties of NiPS_3 , we performed first-principles calculations with Quantum-ESPRESSO⁴⁷. Figure 5(a) shows the calculated band structure of pristine NiPS_3 , where we could see an isolated narrow conduction band which is dominated by the Ni-d orbitals (d_{zx} , d_{zy} , and d_{xy}) and contributed by S-p orbitals. Without doping, the electronic bands are spin degenerate. Inner-chain magnetic order is ferromagnetic carrying a magnetic moment of $1.51 \mu_B$ per Ni atom, and the inter-chain magnetic order is antiferromagnetic as shown in Figure 1(a), which agrees well with previous studies.

Figure 5(b) shows atom projected density of states (PDOS) of NiPS_3 with different doping concentrations, which illustrates the evolution of the electronic structure as a function of doping levels. With light doping concentration of 0.1 electrons/cell, no change occurs on the band. With moderate doping concentrations of 0.2-0.5 electrons/cell, we could see obvious splitting on both orbitals and spin states, and the splitting gets larger with doping concentration increased. With further increasing doping concentration to above 0.6 electrons/cell, the spin-polarization disappears and the system goes back to zigzag AFM order, while the splitting of orbitals still exists. The vanishing of spin-polarization is due to the rise of super-exchange between the two zigzag chains through the S-p states.

To understand the variation of magnetic structures with doping concentrations, we further calculated the orbital-resolved band structure (right panel in Figure 5(a)) and projected density of states (PDOS) of Ni atom on each ferromagnetic chain with opposite orientation of magnetic moments (Ni(1) site and Ni(2) site) at different doping concentrations (as shown in Figure 5(c)). Interestingly, we could see that the splitting causes the doped electrons to occupy Ni atoms at one zigzag ferromagnetic chain with moderate doping concentration of 0.2-0.5 electrons/cell, and a net magnetic moment shows up (discuss in details later). This phenomenon may be understood from Stoner model, which is based on the competition between kinetic energy and exchange energy and is common in material with narrow conduction band. From the calculations, we

could see that the conduction band minimum (CBM) is dominated by d_{zx} , d_{zy} , and d_{xy} orbitals of Ni atoms. As doping concentration increases, due to the electron correlation, the d_{zy} orbital is further pushed up and the CBM is then dominated by d_{zx} and d_{xy} orbitals, which are mainly overlapped in the inter-chain direction, and the overlapping is responsible for the doped electrons to be inter-chain itinerant and lead to Stoner effect induced inter-chain spin splitting.

In fact, NiPS₃ is a self-doped insulator³¹, the S atoms that separate the Ni chains are not fully occupied. Therefore, after doping electrons, the not fully occupied S-p orbital provides a channel for the electrons to be itinerant between the Ni chains. Further, the feature of narrow bands of d orbital makes the density of states large, which is necessary for the Stoner splitting of the itinerant electrons between the Ni chains. With light doping, even though the electrons is inter-chain itinerant, the small DOS close to the CBM is not able to trigger the Stoner effect. However, we could see that the DOS is sharp near the CBM. With doping concentration increases, the DOS on Fermi level increases quickly. When the doping concentration increases to 0.2 electrons/cell, the DOS at Fermi level is large enough to result in Stoner splitting. Thus, the doped electrons only occupy one Ni chain, which results in the net magnetic moment we found in experiment. However, when the doping concentration further increases to over 0.6 electrons/cell, the super-exchange between the chains through the S 2p orbital starts to dominate the magnetic order. Because the d orbital of Ni is more than half occupied, the super-exchange effect leads to antiferromagnetic order between chains and the net magnetic moment disappears. Figure 5(d) shows the magnetic moments on Ni(1) and Ni(2) with different doping concentrations, and the right panel in Figure 1(a) shows a schematic of the magnetic moments on Ni(1) and Ni(2) at moderate doping level, which give a more direct picture of the evolution of the magnetic order of the two chains. At an appropriate doping concentration, the antiferromagnetically coupled two zigzag ferromagnetic chains carry unequal magnetic moments, which leads to the net magnetic moments and FIM characteristics in intercalated THA-NiPS₃.

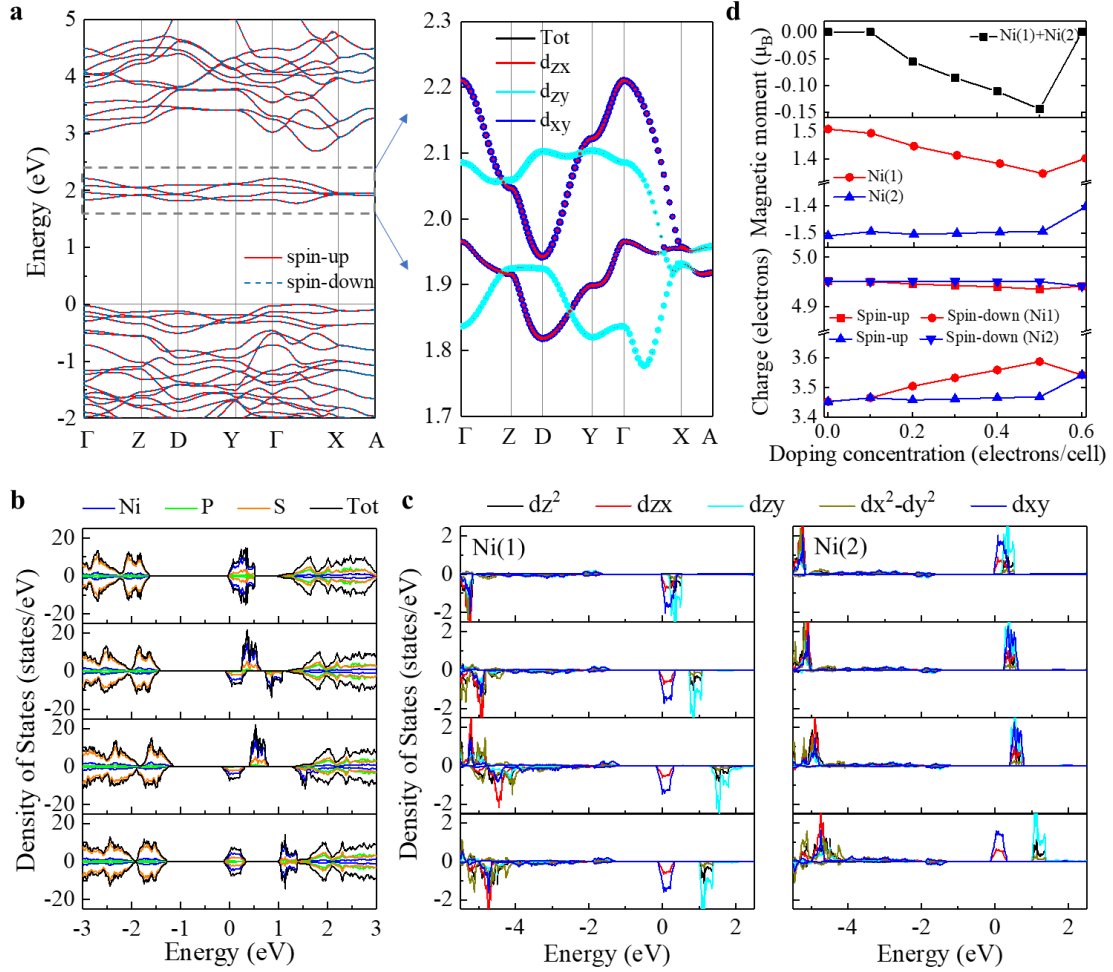


Fig. 5 Band structures and electronic properties of NiPS₃ at different doping concentrations. **a** Band structure of spin-up and spin-down configurations of pristine NiPS₃ (left) and enlarged region of conduction band minimum (right), the orbital characters of bands are represented by different colors. **b** Element-resolved projected density of states (PDOS) of NiPS₃ with doping concentrations of 0.1, 0.2, 0.5 and 0.6 electrons/cell from top to bottom. **c** Ni's d orbital resolved PDOS with doping concentrations of 0.1, 0.2, 0.5 and 0.6 electrons/cell from top to bottom of Ni (1) (left) and Ni (2) (right). **d** Net magnetic moments (top), magnetic moments of Ni (1) and Ni (2) (middle) and charges of Ni (1) and Ni (2) with spin-up and spin-down configurations (bottom) as a function of doping concentrations. A doping concentration of 0.1 electrons/cell corresponds to an electron density of $0.8 \times 10^{13} \text{ cm}^{-2}$.

We further quantitatively compare the experimental results with the calculated theoretical values. The observed FIM signal of THA-NiPS₃ is weak, and the corresponding average net magnetic moment per cell is approximately $0.07 \mu_B$, which lies in the range of theoretically expected values. Due to the highly insulating property of NiPS₃ (conductivity $\sim 10^{-7} \text{ S/cm}$ at room temperature⁴²) and degradation of intercalated NiPS₃ during device fabrication process, quantitative determining the

carrier density in intercalated NiPS₃ is challenging. Previous studies have shown that intercalated THA⁺ cations cause a doping concentration of 0.02 electrons per MoS₂ formula unit³⁷ (corresponding to a carrier density of $2.3 \times 10^{13} \text{ cm}^{-2}$), assuming that intercalated THA⁺ cations cause a similar doping concentration in NiPS₃, which lies in the appropriate doping concentration that leads to the net magnetic moment.

The induced doping concentration is strongly dependent on the species of intercalated organic cations, for example, cations such as tetrabutyl ammonium (TBA⁺), tetrapropyl ammonium (TPA⁺), and cetyltrimethyl ammonium (CTA⁺) cause a substantially large doping concentration ($>10^{14} \text{ cm}^{-2}$) in intercalated 2D materials^{28,37,38}. The conductivity of NiPS₃ increases with increasing doping concentration in lithium intercalated NiPS₃⁴⁸. We measured conductivities of NiPS₃ intercalated with various organic cations (see supplementary Fig. S6). After intercalation, the conductivity of NiPS₃ increases, and the conductivities of TBA-NiPS₃, TPA-NiPS₃ and CTA-NiPS₃ are significantly greater than that of THA-NiPS₃, confirming that intercalated TBA⁺, TPA⁺, and CTA⁺ cations cause a greater doping concentration than intercalated THA⁺ cations. Similar to THA-NiPS₃, the interlayer distance increases to 11.46 Å, 12.14 Å and 14.82 Å for TBA-NiPS₃, TPA-NiPS₃ and CTA-NiPS₃ (as shown in Figure 6(a)), respectively, and the Raman spectra of TBA-NiPS₃, TPA-NiPS₃ and CTA-NiPS₃ also exhibit characteristics of monolayer NiPS₃ sheet (see supplementary Fig. S6(a)). As predicted by our theoretical model that the net magnetic moment disappears at high doping concentration, we do not observe any FIM characteristics in the heavily doped NiPS₃ samples, except a linear dependence of M vs H (as shown in Figure 6(b)). These results rule out the possibility of causing magnetic transition in NiPS₃ by strain, defects and impurity phases, and further confirm the role of carrier doping in tuning the magnetic properties of NiPS₃.

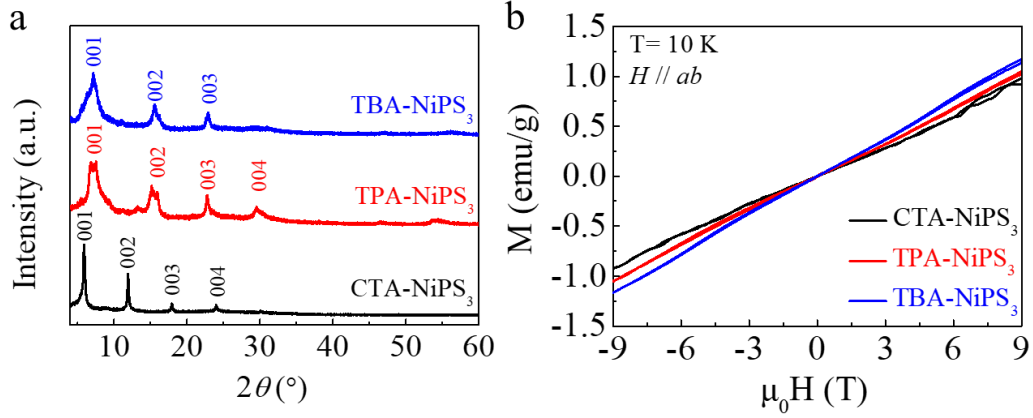


Fig. 6 XRD patterns (a) and field dependence of magnetization (M - H , b) measured under magnetic field $H // ab$ at 10 K of intercalated TBA-NiPS₃, TPA-NiPS₃, and CTA-NiPS₃.

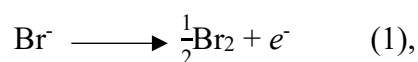
3. Conclusions

We successfully realized the AFM-FIM-AFM transition in NiPS₃ with carrier doping by intercalating organic cations into vdW gaps of NiPS₃. The intercalated organic cations decouple interactions between adjacent layers without introducing defects and impurity phases, and result in electron doping, which significantly alters the electronic and magnetic properties of NiPS₃. At an appropriate doping concentration (which is also achievable by electrostatic gating method), the AFM order in pristine NiPS₃ is switched to the FIM order with $T_c = 100$ K in THA-NiPS₃. At heavy doping concentration (TBA-NiPS₃, TPA-NiPS₃ and CTA-NiPS₃), the AFM order remains again. Such carrier doping tuned magnetic transition is due to the competition between Stoner exchange and super-exchange as the variation of the doping concentration. Our work provides a viable tool to modulate the magnetic properties of vdW magnets by electrical method, and opens a way for investigating strong correlation between electronic structure and magnetic properties of the vdW magnets and designing novel spintronic devices.

Methods

Sample preparation. NiPS₃ crystals were grown by vapor transport method. The mixture of stoichiometric high-purity Ni, P, S (Ni/P/S = 1:1:3) and iodine (10 mg/cm³) as a transport agent were sealed into an evacuated quartz ampule and kept in a two-zone furnace (650 °C - 600 °C) for 1 week. The large single crystals will be harvested in the lower temperature end. Thin flakes of both pristine NiPS₃ and intercalated NiPS₃ were prepared on silicon substrate with a layer of 285 nm SiO₂ by mechanical exfoliation from bulk crystal using adhesive tape.

Electrochemical Intercalation. The electrochemical intercalation of NiPS₃ was carried out in a two-electrode system. The fresh NiPS₃ crystal was fixed on an electrode holder as the negative electrode (cathode), a piece of Pt was used as the positive electrode (anode), and tetraheptyl ammonium bromide (THA⁺Br⁻, Macklin, 98%) dissolved in acetonitrile (Macklin, 99%) at a concentration of 5 mg/ml was used as electrolyte. During the intercalation process, the voltage was slowly swept from 0 V to ~4 V at 50 °C. The electrochemical reaction consists of two half-reactions:



Two bromide ions lose electrons to form Br₂ at the anode, THA⁺ cations are inserted into the vdW gaps of NiPS₃ (cathode), and NiPS₃ receives electrons from the external circuit. Therefore, organic cations intercalation causes electron doping of the sample. Intercalation of other organic cations, such as tetrabutyl ammonium (TBA⁺), tetrapropyl ammonium (TPA⁺), and cetyltrimethyl ammonium (CTA⁺), share the same procedure as the THA⁺.

Characterization. The X-ray diffraction (XRD) patterns were collected by SmartLab® high-resolution X-ray diffractometer (Rigaku, Japan) using Cu K_α radiation, λ = 1.5418 Å. The X-ray photoelectron spectroscopy (XPS) spectra were obtained in Nano-X by PHI-5000 VersaprobeII (Ulvac-Phi, Japan) using Al K_α X-ray (hν=1486.6 eV). The binding energies (BE) were calibrated with respect to the C-C 1 s bond (BE =284.8 eV). Raman spectra were collected by inVia™ confocal Raman microscope (Renishaw) using an excitation wavelength of 532 nm. The magnetic properties were measured by a vibrating sample magnetometer (VSM) of a commercial physical property measurement system (Dynacool-9, Quantum Design).

First-principles density functional theory (DFT) calculations. The Vanderbilt ultrasoft pseudopotential within exchange-correlation potential described by GGA+U, where U = 6 eV is applied on the Ni site⁴⁹. We use the correction of DFT-D to consider the van der Waals interactions between layers⁵⁰. For bulk computations, we construct a supercell of 20 atoms, and 8×5×7 k points mesh generated by Monkhorst-Pack scheme is used. The structure optimizations are performed until the force on each atom is less than 10⁻⁴ Ry/Bohr and the convergence threshold for self-consistency is 10⁻⁸ Ry. The

carrier doping is tuned by changing the total number of electrons adding in the cell, with a compensating jellium background of opposite charge to maintain charge neutrality.

Data availability.

All data supporting the findings of this work are available from the corresponding authors upon request.

References

1. Huang B, *et al.* Layer-dependent ferromagnetism in a van der Waals crystal down to the monolayer limit. *Nature* **546**, 270-273 (2017).
2. Gong C, *et al.* Discovery of intrinsic ferromagnetism in two-dimensional van der Waals crystals. *Nature* **546**, 265-269 (2017).
3. Burch KS, Mandrus D, Park J-G. Magnetism in two-dimensional van der Waals materials. *Nature* **563**, 47-52 (2018).
4. Gong C, Zhang X. Two-dimensional magnetic crystals and emergent heterostructure devices. *Science* **363**, aav4450 (2019).
5. Gibertini M, Koperski M, Morpurgo AF, Novoselov KS. Magnetic 2D materials and heterostructures. *Nat. Nanotechnol.* **14**, 408-419 (2019).
6. Mak KF, Shan J, Ralph DC. Probing and controlling magnetic states in 2D layered magnetic materials. *Nat. Rev. Phys.* **1**, 646-661 (2019).
7. Huang B, *et al.* Emergent phenomena and proximity effects in two-dimensional magnets and heterostructures. *Nat. Mater.* **19**, 1276-1289 (2020).
8. Jiang X, *et al.* Recent progress on 2D magnets: Fundamental mechanism, structural design and modification. *Appl. Phys. Rev.* **8**, 031305 (2021).
9. Li H, Ruan S, Zeng Y-J. Intrinsic van der Waals magnetic materials from bulk to the 2D limit: New frontiers of spintronics. *Adv. Mater.* **31**, 1900065 (2019).
10. Zhang Z, *et al.* Direct photoluminescence probing of ferromagnetism in monolayer two-dimensional CrBr₃. *Nano Lett.* **19**, 3138-3142 (2019).
11. Deng YJ, *et al.* Gate-tunable room-temperature ferromagnetism in two-dimensional Fe₃GeTe₂. *Nature* **563**, 94-99 (2018).
12. Fei ZY, *et al.* Two-dimensional itinerant ferromagnetism in atomically thin Fe₃GeTe₂. *Nat. Mater.* **17**, 778-782 (2018).
13. May AF, *et al.* Ferromagnetism near room temperature in the cleavable van der Waals crystal Fe₃GeTe₂. *ACS Nano* **13**, 4436-4442 (2019).
14. Bonilla M, *et al.* Strong room-temperature ferromagnetism in VSe₂ monolayers on van der Waals substrates. *Nat. Nanotechnol.* **13**, 289-293 (2018).
15. Cai X, *et al.* Atomically thin CrCl₃: An in-plane layered antiferromagnetic insulator. *Nano Lett.* **19**, 3993-3998 (2019).
16. Kim K, *et al.* Suppression of magnetic ordering in XXZ-type antiferromagnetic monolayer NiPS₃. *Nat. Commun.* **10**, 345 (2019).
17. Lee J-U, *et al.* Ising-Type Magnetic Ordering in Atomically Thin FePS₃. *Nano Lett.* **16**, 7433-7438 (2016).

18. Kim K, *et al.* Antiferromagnetic ordering in van der Waals 2D magnetic material MnPS₃ probed by Raman spectroscopy. *2D Mater.* **6**, 041001 (2019).
19. Coak MJ, *et al.* Tuning dimensionality in van-der-Waals antiferromagnetic Mott insulators TMPS₃. *J. Phys. Condens. Matter* **32**, 124003 (2019).
20. Peng Y, *et al.* Magnetic structure and metamagnetic transitions in the van der Waals antiferromagnet CrPS₄. *Adv. Mater.* **32**, 2001200 (2020).
21. Otrokov MM, *et al.* Prediction and observation of an antiferromagnetic topological insulator. *Nature* **576**, 416-422 (2019).
22. Jiang S, Shan J, Mak KF. Electric-field switching of two-dimensional van der Waals magnets. *Nat. Mater.* **17**, 406-410 (2018).
23. Wang Y, *et al.* Strain-sensitive magnetization reversal of a van der Waals magnet. *Adv. Mater.* **32**, 2004533 (2020).
24. Jiang S, Li LZ, Wang ZF, Mak KF, Shan J. Controlling magnetism in 2D CrI₃ by electrostatic doping. *Nat. Nanotechnol.* **13**, 549-553 (2018).
25. Huang B, *et al.* Electrical control of 2D magnetism in bilayer CrI₃. *Nat. Nanotechnol.* **13**, 544-548 (2018).
26. Verzhbitskiy IA, *et al.* Controlling the magnetic anisotropy in Cr₂Ge₂Te₆ by electrostatic gating. *Nat. Electron.* **3**, 460-465 (2020).
27. Wang Z, *et al.* Electric-field control of magnetism in a few-layered van der Waals ferromagnetic semiconductor. *Nat. Nanotechnol.* **13**, 554-559 (2018).
28. Wang NZ, *et al.* Transition from ferromagnetic semiconductor to ferromagnetic metal with enhanced Curie temperature in Cr₂Ge₂Te₆ via organic ion intercalation. *J. Am. Chem. Soc.* **141**, 17166-17173 (2019).
29. Joy PA, Vasudevan S. Magnetism in the layered transition-metal thiophosphates MPS₃ (M=Mn, Fe, and Ni). *Phys. Rev. B* **46**, 5425-5433 (1992).
30. Wildes AR, *et al.* Magnetic structure of the quasi-two-dimensional antiferromagnet NiPS₃. *Phys. Rev. B* **92**, 224408 (2015).
31. Kim SY, *et al.* Charge-spin correlation in van der Waals antiferromagnet NiPS₃. *Phys. Rev. Lett.* **120**, 136402 (2018).
32. Yan M, *et al.* Correlations in the electronic structure of van der Waals NiPS₃ crystals: An X-ray absorption and resonant photoelectron spectroscopy study. *J. Phys. Chem. Lett.* **12**, 2400-2405 (2021).
33. Chittari BL, *et al.* Electronic and magnetic properties of single-layer MPX₃ metal phosphorous trichalcogenides. *Phys. Rev. B* **94**, 184428 (2016).
34. Li X, Wu X, Yang J. Half-metallicity in MnPSe₃ exfoliated nanosheet with carrier doping. *J. Am. Chem. Soc.* **136**, 11065-11069 (2014).
35. Zhou J, *et al.* Layered intercalation materials. *Adv. Mater.* **33**, 2004557 (2021).
36. Wang C, *et al.* Monolayer atomic crystal molecular superlattices. *Nature* **555**, 231-236 (2018).
37. He Q, *et al.* In situ probing molecular intercalation in two-dimensional layered semiconductors. *Nano Lett.* **19**, 6819-6826 (2019).
38. Shi MZ, *et al.* Organic-ion-intercalated FeSe-based superconductors. *Phys. Rev. Mater.* **2**, 074801 (2018).
39. Zhang H, *et al.* Enhancement of superconductivity in organic-inorganic hybrid topological materials. *Sci. Bull.* **65**, 188-193 (2020).

40. Bao W, *et al.* Approaching the limits of transparency and conductivity in graphitic materials through lithium intercalation. *Nat. Commun.* **5**, 4224 (2014).
41. Susner MA, Chyasnachyus M, McGuire MA, Ganesh P, Maksymovych P. Metal thio- and selenophosphates as multifunctional van der Waals layered materials. *Adv. Mater.* **29**, 1602852 (2017).
42. Kuo C-T, *et al.* Exfoliation and raman spectroscopic fingerprint of few-layer NiPS₃ van der Waals crystals. *Sci. Rep.* **6**, 20904 (2016).
43. Foot PJS, *et al.* The structures and conduction mechanisms of lithium-intercalated and lithium-substituted nickel phosphorus trisulphide (NiPS₃), and the use of the material as a secondary battery electrode. *Phys. Stat. Sol. (a)* **100**, 11-29 (1987).
44. Basnet R, Wegner A, Pandey K, Storment S, Hu J. Highly sensitive spin-flop transition in antiferromagnetic van der Waals material MPS₃ (M=Ni and Mn). *Phys. Rev. Mater.* **5**, 064413 (2021).
45. Cong X, Liu X-L, Lin M-L, Tan P-H. Application of Raman spectroscopy to probe fundamental properties of two-dimensional materials. *npj 2D Mater. Appl.* **4**, 13 (2020).
46. Currò GM, Grasso V, Neri F, Silipigni L. The effects of the lithium intercalation on the X-ray photoelectron spectra of NiPS₃. *Il Nuovo Cimento D* **17**, 37-52 (1995).
47. Giannozzi P, *et al.* QUANTUM ESPRESSO: a modular and open-source software project for quantum simulations of materials. *J. Phys. Condens. Matter* **21**, 395502 (2009).
48. Giunta G, Grasso V, Neri F, Silipigni L. Electrical conductivity of lithium-intercalated thiophosphate NiPS₃ single crystals. *Phys. Rev. B* **50**, 8189-8194 (1994).
49. Cococcioni M, de Gironcoli S. Linear response approach to the calculation of the effective interaction parameters in the LDA+U method. *Phys. Rev. B* **71**, 035105 (2005).
50. Grimme S. Semiempirical GGA-type density functional constructed with a long-range dispersion correction. *J. Comput. Chem.* **27**, 1787-1799 (2006).

Acknowledgements

This work was supported by the National Natural Science Foundation of China (Grant Nos. 92065206, 11974211), the Natural Science Foundation of Shandong Province (Grant No. ZR2020MA071), and the Qilu Young Scholar Program of Shandong University.

Author contributions

Y.L.W. conceived the project. B.S. grew bulk NiPS₃ crystals. M.J.M. performed the electrochemical intercalation, Raman, and AFM measurements under the supervision of Y.L.W.. S.L.W. and M.J.M. performed the VSM measurements under the supervision of S.P.W., B.L.H. and Y.L.W.. X.W.Z. performed the first-principles calculations under the supervision of X.H.L. M.J.M., Y.Z., H.N.S performed XRD measurements under the supervision of Y.X.C.. M.J.M. performed XPS measurements under the supervision of F.S.L.. M.J.M., L.X.Y., H.X. performed electrical conductivity measurements. M.J.M., X.W.Z., X.H.L., and Y.L.W. wrote the manuscript, and all authors participated in discussing the results and revising the manuscript.

Competing interests: The authors declare no competing interests.